Dual-Focal Metalenses Based on Complete Decoupling of Amplitude, Phase, and Polarization

He-Xiu Xu[1,2], Menghua Jiang[2], Guangwei Hu[2], Lei Han[2], Ying Li[2], and Cheng-Wei Qiu[2]

[1]Air Force Engineering University
Xi'an, 710051, China
E-mail: hxxuellen@gmail.com

[2]Department of Electrical and Computer Engineering
National University of Singapore
Singapore 117583, Singapore

Abstract

The simultaneous control of amplitude and phase via metasurfaces affords us an unprecedented degree of freedom in manipulating electromagnetic waves. However, currently most designs suffer from low efficiency, which raises certain concerns for real-world applications. Moreover, complete amplitude, phase, and polarization modulation is particularly challenging. This typically requires a combination of attenuators, optically thick wave plates, and large dielectric lenses. Here, we propose an alternative scheme by introducing vertical-mode cross-coupling for polarization control and high efficiency, while involving spatially-varied orientations and structures for independent amplitude and phase modulation. The vertical-mode cross-coupling is synthesized by stacking triple-layer twisted split-ring resonators (SRRs) operated in a transmissive scheme. Such tight cross-coupling and chirality-assisted coherent multiple resonances facilitate high cross-polarization conversion efficiency (~100%) and a broadband transmission window with full phase coverage. As a proof of concept, two dual-focal metalenses that are challenging to be actualized through conventional metasurfaces were designed and studied numerically and experimentally, with a total thickness of $\lambda_0/12$ at microwave frequencies. Desirable dual-focusing behavior with axial and lateral alignment of two foci were demonstrated. Our findings, not confined to microwave operation, open up an alternative way to the fine control of light, and can stimulate novel and high-performance versatile photonic metadevices.

1. Introduction

The explosive field of metasurfaces has afforded extraordinary capabilities for manipulating electromagnetic (EM) waves [1-7]. Metasurfaces, composed of a mass of sub-wavelength-spaced meta-atoms, has generated huge interest from both the physics and engineering communities, due to their exotic behavior and promising applications. The local amplitude, phase, and polarization are three types of important information for the control of the output EM wavefront. In general, previous pursuits of metasurfaces can be divided into these three categories. However, the simultaneous modulation of the above three items has rarely been reported. In recent years, we have witnessed some progress toward simultaneous amplitude and phase control [8-10]. However, most attempts were either in reflection geometry or with low conversion efficiency, the maximum of which was fundamentally restricted to 25%, which may seriously hinder real-world applications. Moreover, all these designs left the polarization control totally irrelevant or essentially unaddressed. On the other hand, much attention has been paid to high-efficiency operation, which is critically important for high-performance photonic devices [11]. However, all these designs were confined to phase- or polarization-only modulation, making kaleidoscopic wavefront control particularly challenging.

Here, we propose a scheme [12] that is capable of *complete* amplitude, phase, and polarization modulation with high efficiency in transmission geometry, opening up fascinating opportunities to go beyond what is achievable by available metasurfaces. By introducing a set of vertical coupling modes, near 100% efficiency is actualized by a *total* cross-polarization conversion between the incident and transmitted beam. Most importantly, the transmission amplitude can be continuously tuned by altering the orientation angle without changing the local phase response. Such exotic merit allows decoupling of the fixed relationship between the phases and magnitudes, which can be engineered for kaleidoscopic wavefront shaping.

2. Principle and Properties of the Anisotropic Meta-Atom

For full-space EM wave manipulation by a thin metasurface (the left panel of Figure 1a), four parameters – r_{uu}, r_{vu}, t_{uu}, and t_{vu}, with u and v denoting the two principle axes – are typically involved to completely describe the metasurface's reflection and transmission properties. Because of symmetry requirements, half of the coupled energy is radiated back, leading to a fundamentally limited cross-polarized efficiency below 25% for single-layer metasurfaces. Although inclusion of effective magnetic responses to the meta-atom assists high co-polarized transmissions [11], it is inefficient for polarization modulation due to the coherent electric and magnetic response. Completely different from previous methods, we here propose a scheme by introducing vertical interlayer mode cross-coupling and coherent multiple resonances. Full cross-polarization conversion can be engineered with the three residual components completely suppressed, facilitating a near 100% transmission rate, as shown in the right panel of Figure 1a.

To realize complete cross-polarization conversion, the planar meta-atom should exhibit strong local chirality, without any mirror or rotational symmetry or the three-dimensional chiral architectures [13]. Such structural chirality yields strong cross-coupling between electric and magnetic fields that occurs at resonances. Having these aspects in mind, the basic building block for complete decoupling of amplitude, phase, and polarization was designed and is shown in Figure 1b. The transmissive meta-atom consists of triple-twisted split ring resonators (SRRs) sandwiched by two dielectric spacer layers with a dielectric constant (ε_r) of 4.5 and a thickness (h) of 1.5 mm. Each pair of neighboring SRR metallic patterns has a mutual twist angle of $\Phi = 45°$. Such a judicious choice as discussed in the following offers resonance hybridization and interlayer coupling, which are the keys for polarization transformation. By shining the composite meta-atom from the bottom with a y-polarized plane wave, triple resonant modes can be coherently excited, accounting for the three resonant peaks with almost 100% efficiency and dips manifested across the $|t_{yy}|$ or $|t_{xx}|$ (Figure 1c) spectrum. These coherently excited resonant modes, identified from the field/current distributions shown in the inset of Figure 1c, in order

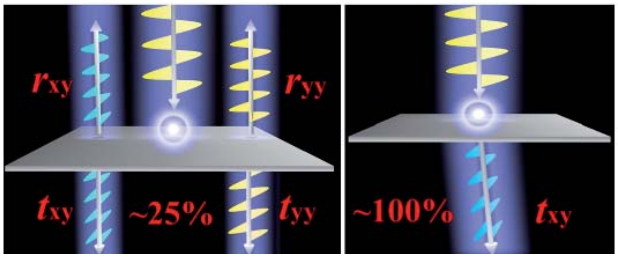

Figure 1a. A conceptual illustration to overcome the low efficiency in previous single-layer metasurfaces and a characterization of the proposed transmissive triple-layer meta-atom with 90° polarization conversion: a schematic diagram.

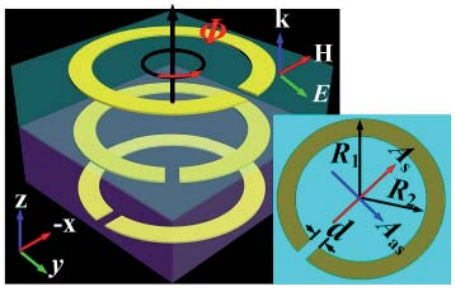

Figure 1b. The topology and a parametric illustration for the case of Figure 1a.

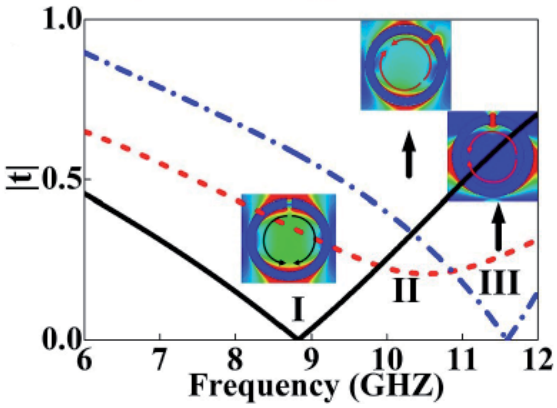

Figure 1c. The FDTD simulated co-polarization transmission spectrum and field/current distributions of three individual SRR_1, SRR_2, and SRR_3 cases to identify three fundamental resonant modes.

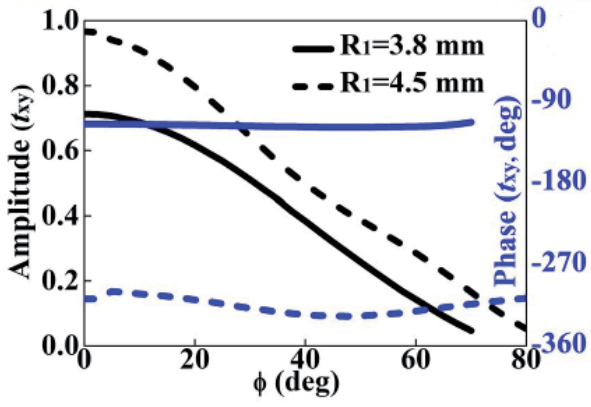

Figure 1d. The FDTD-calculated transmission amplitude and phase responses of t_{xy} as a function of the orientation angle, Φ. The results of both meta-atoms with $R_1 = 4.5$ mm and $R_1 = 3.8$ mm are given.

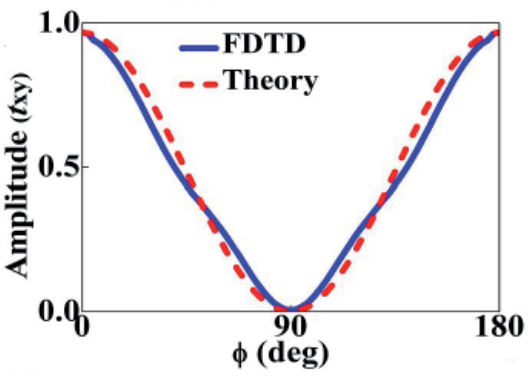

Figure 1e. The theoretically calculated transmission amplitude and phase responses of t_{xy} as a function of the orientation angle, Φ. Only the meta-atom with $R_1 = 4.5$ mm was selected for verification.

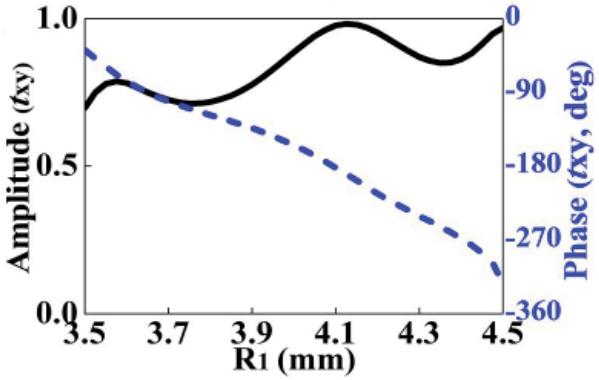

Figure 1f. The FDTD-calculated transmission amplitude and phase as a function of R_1 at 9.45 GHz.

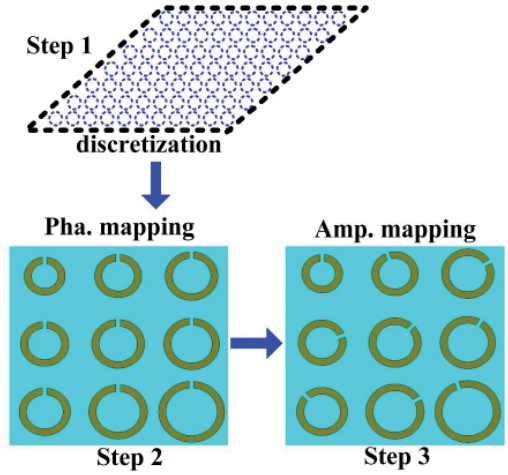

Figure 1g. An illustration of the three-step design process. In all cases, the meta-atoms had $d = 0.6$ and a square lattice constant of 10 mm × 10 mm.

correspond to the symmetric dipolar-resonant (I), hybrid (II), and asymmetric (III) LC-resonant modes of three SRRs with $\Phi = 0°$ (SRR_1), $\Phi = 45°$ (SRR_2), and $\Phi = 90°$ (SRR_3), respectively from low to high frequencies.

The cascading and superposition of these multiple resonant modes facilitates the broadband cross-polarization transmission window, and also increases the discontinuous phase coverage without affecting the constant transmission amplitude. By coherently varying the radii (R_1 and R_2) of the above triple SRRs, the desirable full phase coverage of t_{xy} can be engineered. Here, the width of the SRRs, $w = 1$ mm, is kept constant for a simple design. Most importantly, continuous amplitude variation is actualized from zero to unity by tuning the orientation angle, Φ, of the SRRs without altering the phase response in the transmission window. The merit of this – which may fin critical applications in the synthesis of complex wave fields, novel beam shaping, and high-quality holographic images – was further proven from the results shown in Figure 1d, where the transmission spectrum is plotted as a function of Φ and a maximum phase change of 22° was demonstrated. Such a Φ-immune phase response brings extreme flexibility in reshaping the wavefront through individually altering the orientation angles and structure parameters. We obtained the $\varphi - R_1$ relationship based on full-wave FDTD simulations, since the transmission phase of t_{xy} as a function of R_1 was fully numerical. Intriguingly, we found that the transmission amplitude of t_{xy} could be derived analytically as a function of Φ (see the following). Such theoretical prediction avoids much time-consuming parametric analyses in metadevice design.

The analytical derivation starts with the symmetric and anti-symmetric mode analysis of a single-layer SRR with an open split directed toward Φ relative to the x axis. For a normally incident x-polarized plane wave, symmetric ($E_s^{out} = E_x^{in} \cos\Phi A_s e^{i\varphi_s}$) and anti-symmetric ($E_{as}^{out} = E_x^{in} \sin\Phi A_s e^{i\varphi_{as}}$) modes are simultaneously excited, and are decoupled into x- and y-polarized components as

$$E_x^{out} = E_x^{in}\left(A_s e^{i\varphi_s}\cos^2\Phi + A_{as}e^{i\varphi_{as}}\sin^2\Phi\right), \quad (1)$$

$$E_y^{out} = \frac{1}{2}E_x^{in}\sin 2\Phi\left(A_s e^{i\varphi_s} - A_{as}e^{i\varphi_{as}}\right). \quad (2)$$

Similarly, the output x- and y-polarized components under a normally incident y-polarized plane wave can be expressed as

$$E_x^{out} = \frac{1}{2}E_y^{in}\sin 2\Phi\left(A_s e^{i\varphi_s} - A_{as}e^{i\varphi_{as}}\right), \quad (3)$$

$$E_y^{out} = E_y^{in}\left(A_s e^{i\varphi_s}\sin^2\Phi + A_{as}e^{i\varphi_{as}}\cos^2\Phi\right). \quad (4)$$

By taking Φ as $\Phi = 0°$, $\Phi = 45°$, and $\Phi = 90°$ we immediately obtain the output components for the three individual single-layer SRRs. The output components for the whole bottom-to-top SRRs can then be derived by cascading these transmission matrixes and taking the outputs of the former SRRs as new inputs of the latter SRRs. After a complicated derivation, we eventually obtain the output *x*- and *y*-polarized components of the triple-layer meta-atom under *x* polarization as

$$E_y^{out} = \frac{1}{8} E_x^{in} A\left[\cos 2\Phi\left(A^2 + B^2\right) + 2AB\right], \quad (5)$$

$$E_x^{out} = \frac{1}{8} E_x^{in}\left[-\left(AB^2 + A^3\right)\sin 2\Phi + B^3 - A^2 B\right]. \quad (6)$$

Here, $\alpha = A_s e^{i\varphi_s}$, $\beta = A_{as} e^{i\varphi_{as}}$, $A = \alpha - \beta$ and $B = \alpha + \beta$. Based on the same procedure, the *x* and *y*-polarized outputs under *y*-polarized excitation are formulized as

$$E_y^{out} =$$

$$\frac{1}{8} E_y^{in}\left[\left(B^2 - A^2\right)B - \left(B^2 A - A^3\right)\sin 2\Phi - 2A^3 \sin^3 2\Phi\right] (7)$$

$$E_x^{out} =$$

$$\frac{1}{8} E_y^{in} A\left[-2AB - 2A^2 \cos^3 2\Phi + \left(3A^2 + B^2\right)\cos 2\Phi\right] \quad (8)$$

For verification, we theoretically calculated the output components of the triple-layer meta-atom with $R_1 = 4.5$ mm and compared them with the full-wave FDTD simulation results in Figure 1e. Satisfactory agreement and accuracy of the analytical results was observed, which offers a quick way to relate rotation angles of the meta-atom to specific transmission amplitudes.

With the above results and features of our meta-atom, the design of the metasurface with arbitrary amplitude and phase distribution for prescribed functionality is simple. This typically involves three steps, as shown in Figure 1g. First, the required two-dimensional amplitude and phase profiles across the aperture at the operating frequency f_0 are determined. Second, the metasurface layout is mapped out by determining R_1 for each meta-atom according to the target phase profile and $\varphi - R_1$ relation shown in Figure 1f. Third, the design is finalized by spatially rotating each meta-atom with Φ by following the destined amplitude profile and analytical $t - \Phi$ relation. Our strategy with full Φ-dependent amplitude modulation, even in a cascaded profile, is still very thin, with a thickness of only $\lambda_0/12$, which is very suitable for integrated flat photonic devices.

Figure 2a. The design, theoretical, and numerical characterization of the first bifocal metalens with lateral alignment of two foci: a top view of half the metalens layout with a total of $M \times N = 16 \times 1$ pixels distributed along the *x* and *y* axes.

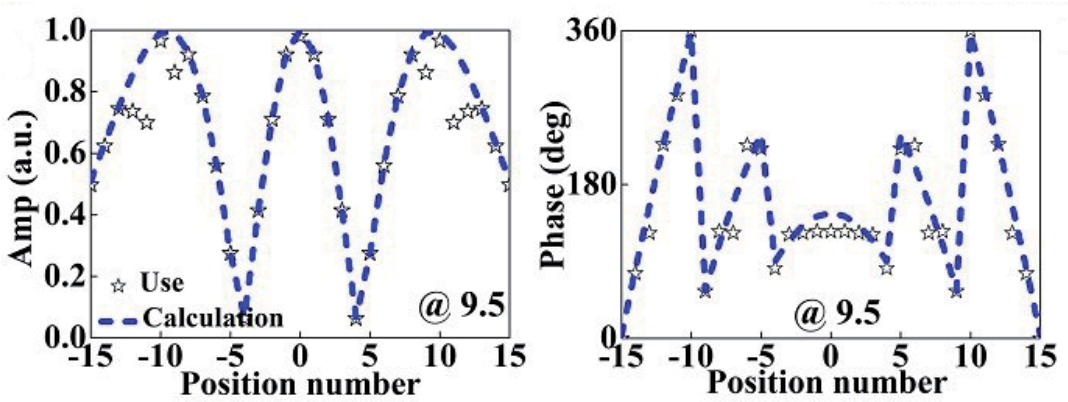

Figure 2b. The required (blue dashed) and digitized (pentacle) normalized amplitudes (left) and phases (right) of the designed lateral bifocal metalens in the one-dimensional case.

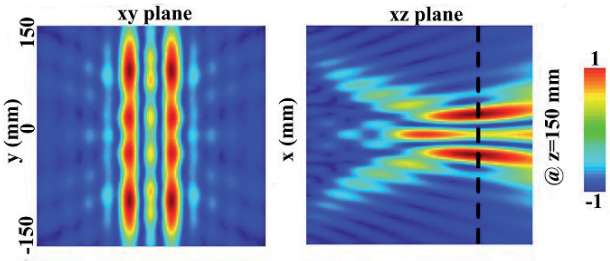

Figure 2c. The theoretically calculated E-field distributions in the *xy* (left) and *xz* (right) planes for the one-dimensional case at 9.5 GHz.

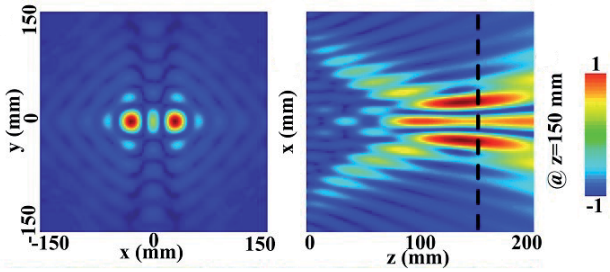

Figure 2e. The theoretically calculated E-field distributions in the *xy* (left) and *xz* (right) planes for the two-dimensional case at 9.5 GHz.

3. Bifocal Metalens with Lateral or Axial Alignment of Two Foci

We demonstrated the possible applications of our flexible metasurface by designing and examining two bifocal metalenses with lateral or axial alignment of two foci. For these purposes, the required phase and amplitude profiles across the aperture should fulfill the following conditions:

$$\sigma(x,\lambda) = \alpha_1 e^{j\frac{2\pi}{\lambda}\left[\sqrt{(x-d/2)^2+F^2}-F\right]} + \alpha_2 e^{j\frac{2\pi}{\lambda}\left[\sqrt{(x+d/2)^2+F^2}-F\right]}, \quad (9a)$$

$$\sigma(x,\lambda) = \alpha_1 e^{j\frac{2\pi}{\lambda}\left(\sqrt{x^2+F_1^2}-F_1\right)} + \alpha_2 e^{j\frac{2\pi}{\lambda}\left(\sqrt{x^2+F_2^2}-F_2\right)}. \quad (9b)$$

Here, λ was the designed wavelength at $f_0 = 9.5$ GHz, α_1 and α_2 were the strengths of the two foci, $F = 150$ mm was the focal point, $d = 60$ mm was the lateral distance between the two foci of the first metalens, and $F_1 = 55$ mm and $F_2 = 130$ mm were the two axial focal points of the second metalens. Both lenses were targeted at 9.5 GHz with $\alpha_1 = \alpha_2 = 0.5$.

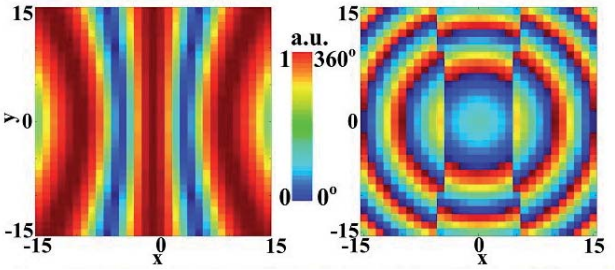

Figure 2d. The required (blue dashed) and digitized (pentacle) normalized amplitudes (left) and phases (right) of the designed lateral bifocal metalens in the two-dimensional case.

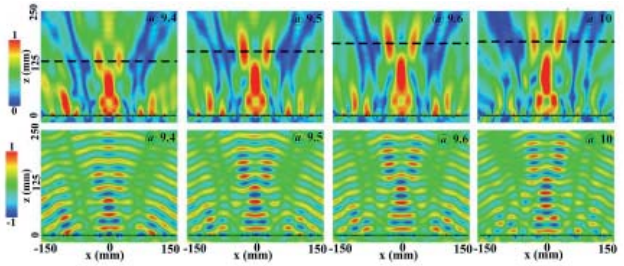

Figure 2f. The numerically simulated E_x distributions for both $\mathrm{Mag}(E_x)$ (top row) and $\mathrm{Re}(E_x)$ (bottom row) at several representative frequencies.

Figure 2 plots the layout and exotic properties of the first metalens exhibiting dual lateral foci based on performing both theoretical predictions and full-wave FDTD simulations, where we illuminated the metalens with normally a incident *y*-polarized plane wave along the *z* direction and recorded the scattered *x*-polarized radiation. Since it is not easy to realize all-level amplitude and phase patterns, we utilized six-level (pentacle) phase modulation to digitize the required full profiles (dashed) in the one-dimensional case. Each level corresponded to a meta-atom with specific radius, as portrayed in Figure 2a, and the orientations of these were determined with minimum amplitude tolerances as shown in Figure 2b. More design details for each pixel can be found in Table 1. Consistent amplitude and phase profiles could be appreciated between the full and digitized values. As could be seen from Figures 2c, 2e, and 2f, the prescribed dual-focusing behavior with lateral alignment of two foci along the *x* direction with $d = 59$ mm were evidently obtained from the theoretical results of both the one-dimensional and two-dimensional metalenses. Due to the passive dispersion, the FDTD simulated foci (dashed line) continuously increased, and the two focal intensities became slightly asymmetric as the frequency went beyond f_0. The beamwidth of the two foci measured by the FWHM of the field patterns along the dashed line was approximately 22 mm at 9.5 GHz.

Figure 3 shows the properties of the second bifocal metalens with axial alignment of two foci. Both one-dimensional and two-dimensional metalenses were theoretically designed with their amplitude and phase patterns shown in Figure 3b and 3d. More design details for

Table 1. Detailed design information for the bifocal metalens I with lateral alignment of two foci.

Amplitude	0.6	0.64	0.68	0.7	0.76	0.78	0.78	0.78	0.73	0.65	0.49	0.23	0.16	0.6	0.95	0.9
Phase	109°	206°	301°	34.5°	125°	212°	295°	12.9°	84.6°	149°	203°	247°	99.3°	118°	124°	119°
Types	5	7	9	2	5	7	9	1	3	6	7	8	4	5	5	5
***R* (mm)**	4.18	3.78	3.5	4.45	4.18	3.78	3.5	4.49	4.29	4.08	3.78	3.6	4.23	4.18	4.18	4.18
Φ	38°	16°	0°	26°	28°	0°	0°	20.8°	26°	33°	31°	50°	67°	37°	0°	0°
Amplitude	0.6	0.65	0.7	0.73	0.75	0.7	0.7	0.78	0.73	0.65	0.5	0.23	0.17	0.6	0.97	0.97
Phase	120°	209°	285°	24.5°	115°	209°	285°	9 °	81.4°	145°	206°	233°	96.7°	114°	118°	118°

Note: The theoretically required amplitude and phase profiles are given in the top two rows while, the practically utilized profiles are listed in the bottom two rows. Moreover, the spatially varied R and Φ for each meta-atom are marked in yellow. As shown, reasonable agreement of amplitude and phase patterns was observed between the two cases, enabling a simple design without severely sacrificing the performance of these metalenses.

each pixel can be found in Table 2. In the realization of the one-dimensional lens with the layout shown in Figure 3a, nine-level (pentacle) phase modulations were cautiously performed to digitize the required full one-dimensional phase profile (dashed) depicted in Figure 3b. Again, both theoretical (Figures 3c and 3e) and FDTD (Figures 3f-3h) results agreed well, implying desirable dual focusing from the two localized spots with maximum intensity along the

Figure 3a. The design, theoretical, and numerical characterization of the second bifocal metalens with axial alignment of two foci: the top view of the metalens layout with a total of $M \times N = 31 \times 1$ pixels distributed along the x and y axes.

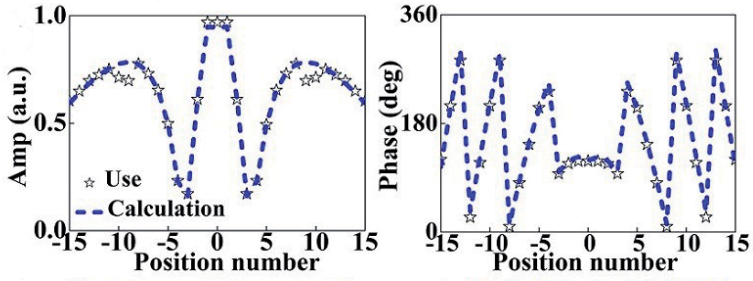

Figure 3b. The required (blue dashed) and digitized (pentacle) normalized amplitudes (left) and phases (right) of the designed lateral bifocal metalens in the one-dimensional case.

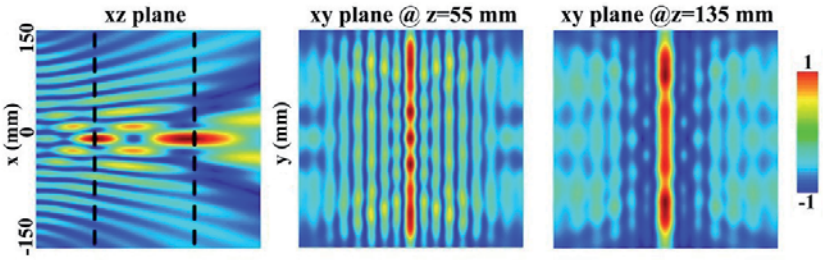

Figure 3c. The theoretically calculated E-field distributions in the *xz* (left) and *xy* (right) planes for the one-dimensional case at 9.5 GHz.

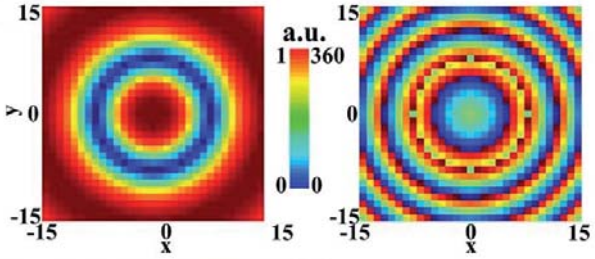

Figure 3d. The required (blue dashed) and digitized (pentacle) normalized amplitudes (left) and phases (right) of the designed lateral bifocal metalens in the two-dimensional case.

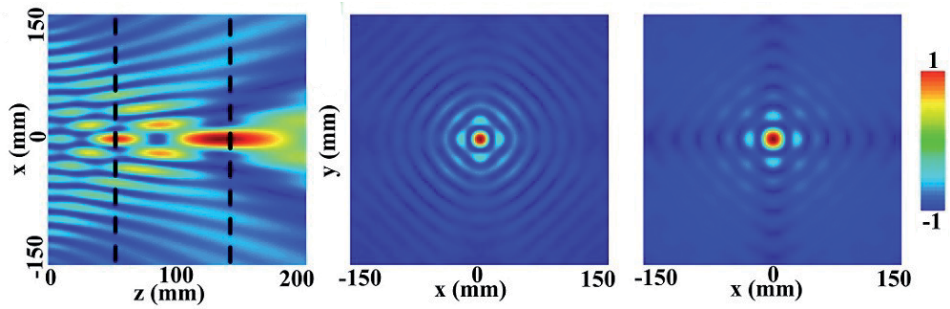

Figure 3e. The theoretically calculated E-field distributions in the *xz* (left) and *xy* (right) planes (at $z = 55$ mm and $z = 135$ mm) for the two-dimensional case at 9.5 GHz.

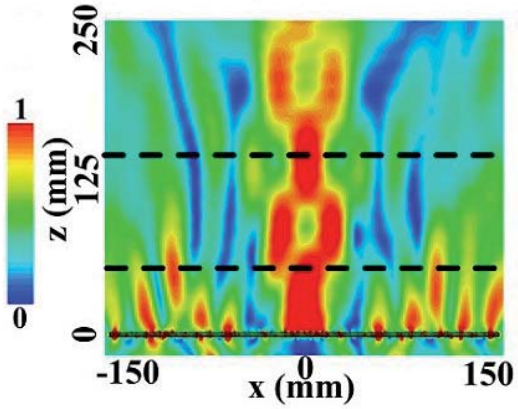

Figure 3f. The numerically simulated E_x distributions for both $\mathrm{Mag}(E_x)$ (top row) and $\mathrm{Re}(E_x)$ (bottom row) at 9.4 GHz and 9.5 GHz.

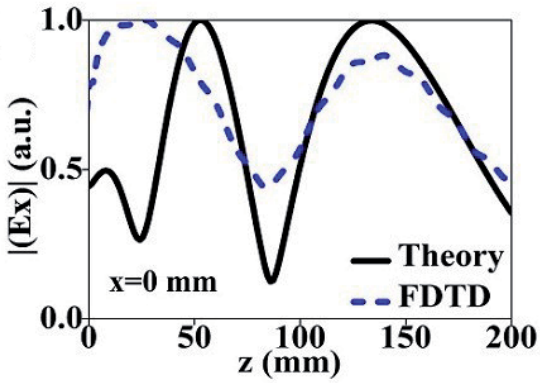

Figure 3g. A comparison of E_x between theoretical and FDTD calculations at 9.4 GHz and 9.5 GHz.

optical axis (*z* axis). Some deviations observed in the FDTD calculations, especially for the non-identical focal intensity at the two foci, were probably induced by the inherently different focusing capability of the finite-size lens at different positions, and the phase/amplitude discrepancies between the utilized meta-atoms and the ideal meta-atoms.

We finally fabricated the first metalens to prove the dual-focusing capability. The metalens sample with the photograph shown in Figure 4a was composed of $M \times N = 31 \times 25$ pixels, with spatially varied structures and orientations. Figure 4b depicts the measured two-dimensional contour of the near-field E_x by scanning an area of 90 mm × 180 mm in steps of 5 mm. All fields were normalized to their maximum. As expected, two focal spots with extremely localized intensity were obtained near $z = 150$ mm at the observed frequencies. As shown in Figure 4c, good agreement could be observed between

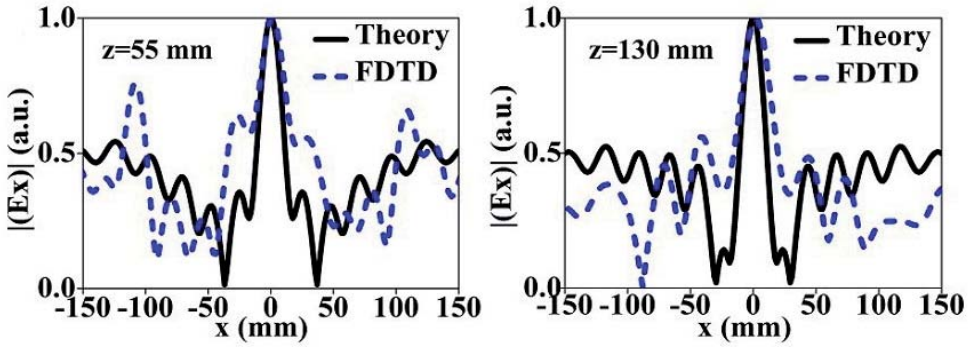

Figure 3h. A comparison between theoretical and FDTD calculations of E_x at the two values of z shown by dashed lines in Figure 3f.

Table 2. Detailed design information for the bifocal metalens II with axial alignment of two foci.

Amplitude	0.51	0.63	0.75	0.86	0.94	0.99	0.99	0.93	0.79	0.57	0.27	0.07	0.41	0.72	0.93	1
Phase	3.3°	80.8°	155°	226°	294°	357°	55.8°	110°	159°	202°	239°	90.1°	114°	132°	143°	146°
Types	1	3	4	5	6	1	2	4	4	5	5	3	4	4	4	4
***R* (mm)**	4.5	4.29	4.15	3.67	3.5	4.5	4.4	4.15	4.15	3.67	3.67	4.29	4.15	4.15	4.15	4.15
Φ	40°	34.5°	28.5°	0°	0°	0°	0°	13.5°	25.5°	27°	47.5°	77°	50°	31°	13.5°	0°
Amplitude	0.5	0.62	0.75	0.74	0.7	0.97	0.86	0.92	0.79	0.56	0.28	0.06	0.41	0.71	0.92	0.98
Phase	0°	76.1°	123°	227°	285°	360°	55.2°	125°	123°	226°	222°	82°	121.4°	123°	125°	125°

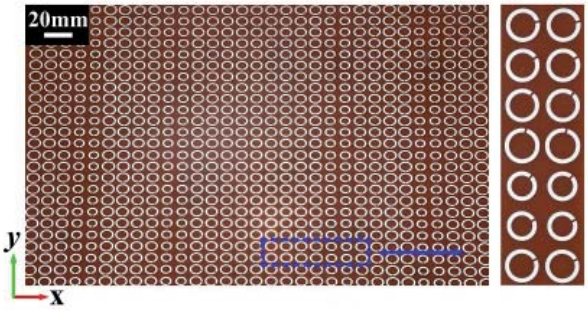

Figure 4a. The experimental characterization of the one-dimensional bifocal metalens with lateral alignment of two foci: a photograph of the fabricated sample with a total of $M \times N = 31 \times 25$ (top view).

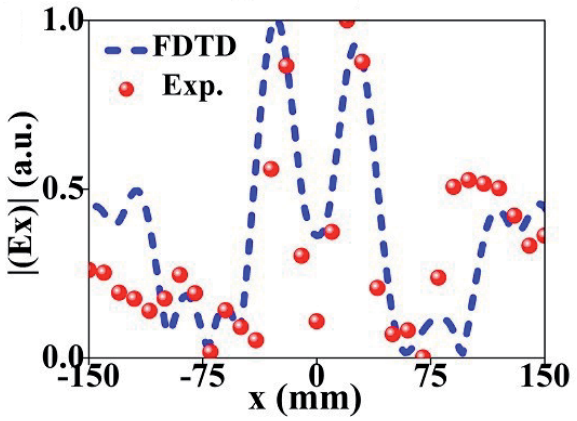

Figure 4c. A comparison of the simulated and measured E_x intensities along the line $z = 150$ mm at 9.5 GHz.

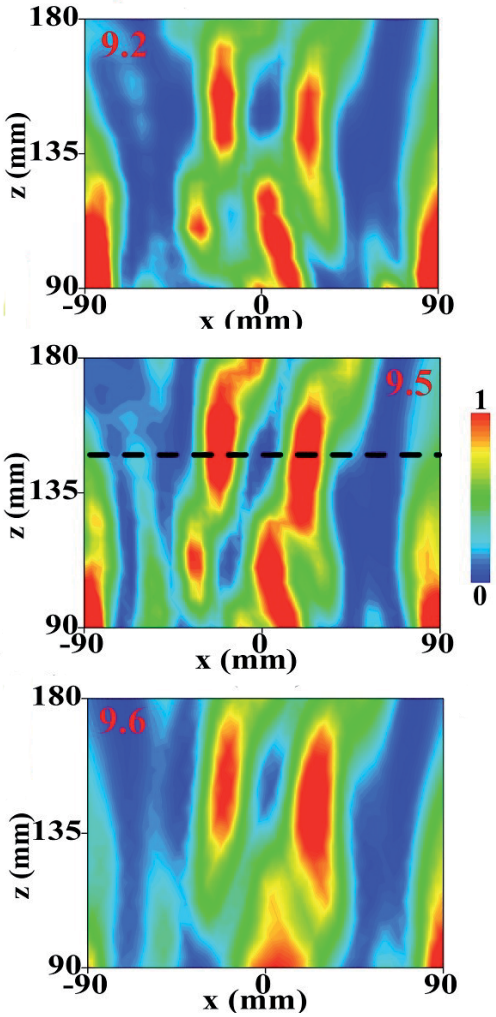

Figure 4b. The experimentally measured E-field (E_x) distributions at 9.2 GHz, 9.5 GHz, and 9.6 GHz.

the theoretical, numerical, and experimental E_x along $z = 150$ mm, indicating measured FWHM beamwidths of 20 mm and 21 mm ($0.63\lambda_0$) for the two foci. The non-ideal alignment of the metalens and the exciting horn gave rise to the slight distortion of the fields, especially for the oblique manifestation of the two foci. Nevertheless, this had little effect on identifying the high-resolution dual-focusing behavior.

4. Conclusion

To sum up, we have proposed and demonstrated an efficient approach for simultaneous manipulation of transmissive polarization, amplitude, and phase with high efficiency from the perspective of analytical derivation, numerical simulation, and experimental demonstration. By stacking triple-layer SRRs with a specific twist angle, vertical-mode cross-coupling was achieved, and thus complete cross-polarization transmission could be engineered within a broad window. Most importantly, the decoupling of changing radius (phase) and orientations (amplitude) afforded us unprecedented degrees of freedom (DOF) for EM wavefront control. For verification, two metalenses that are impossible to realize through phase-only control of conventional metasurfaces were numerically and experimentally investigated with elegant performance.

5. Acknowledgements

This work was supported by the Key Program of Natural Science Foundation of Shaanxi Province (2017KJXX-24); Youth Talent Lifting Project of the China Association for Science and Technology (17-JCJQ-QT-003); China Scholarship Fund (20173059).

6. References

1. N. F. Yu, P. Genevet, M. A. Kats, et al., "Light propagation with phase discontinuities: Generalized laws of reflection and refraction," *Science*, **334**, 2011, pp. 333-337.

2. L. Li, T. J. Cui, W. Ji, S. Liu, J. Ding, X. Wan, Y. B. Li, M. Jiang, C. Qiu, and S. Zhang, "Electromagnetic reprogrammable coding-metasurface holograms," *Nat. Commun.*, **8**, 2017, p. 197.

3. H.-X. Xu, G. Hu, Y. Li, L. Han, J. Zhao, et al., "Interference-assisted kaleidoscopic meta-plexer for arbitrary spin-wavefront manipulation," *Light: Sci. Appl.*, **8**, 2019, p. 3.

4. H.-X. Xu, L. Han, Y. Li, Y. Sun, J. Zhao, et al., "Completely spin-decoupled dual-phase hybrid metasurfaces for arbitrary wavefront control," *ACS Photonics*, **6**, 2019, pp. 211-220.

5. H.-X. Xu, L. Zhang, Y. Kim, G.-M. Wang, K.-X. Zhang, et al., "Wavenumber-splitting metasurfaces achieve multi-channel diffusive invisibility," *Advanced Optical Materials*, **6**, 2018. p. 1800010.

6. H.-X. Xu, S. Tang, C. Sun, L. Li, H. Liu, et al., "High-efficiency broadband polarization-independent super-scatterer using conformal metasurfaces," *Photonics Research*, **6**, 2018, pp. 782-788.

7. H.-X. Xu, S. Ma, X. Ling, X.-K. Zhang, S. Tang, et al., "Deterministic approach to achieve broadband polarization-independent diffusive scatterings based on metasurfaces," *ACS Photonics*, **5**, 2018, pp. 1691-1702.

8. L. Liu, et al. "Broadband metasurfaces with simultaneous control of phase and amplitude," *Adv. Mater.*, **26**, 2014, pp. 5031-5036.

9. Z. Li, H. Cheng, Z. Liu, S. Chen, and J. Tian, "Plasmonic airy beam generation by both phase and amplitude modulation with metasurfaces," *Adv. Opt. Mater.*, **4**, 2016, pp. 1230-1245.

10. Y. Zhu, et al., "Fine manipulation of sound via lossy metamaterials with independent and arbitrary reflection amplitude and phase," *Nat. Commun.*, **9**, 2018, p. 1632.

11. C. Pfeiffer and A. Grbic, "Metamaterial Huygens' surfaces: tailoring wave fronts with reflectionless sheets," *Phys. Rev. Lett.*, **110**, 2013, p. 197401.

12. H.-X. Xu, G. Hu, Y. Li, L. Han, M. Jiang, et al., "Chirality-assisted high-efficiency metasurfaces with independent control of phase, amplitude and polarization," *Advanced Optical Materials*, **7**, 2019, p. 1801479.

13. Y. Zhao, M. A. Belkin, and A. Alù, "Twisted optical metamaterials for planarized ultrathin broadband circular polarizers," *Nat. Commun.*, **3**, 201 2, p. 870.